Enhanced signal-to-noise ratio in magnonic logic gates via dipole coupling

Ryunosuke Hayashi,[1] Shoki Nezu,[1] and Koji Sekiguchi[2,3,4,*]

[1] *Graduate School of Engineering Science, Yokohama National University, Tokiwadai 79-5, Yokohama 240-8501, Japan*

[2] *Institute of Advanced Science, Yokohama National University, Tokiwadai 79-5, Yokohama 240-8501, Japan*

[3] *Institute of Multidisciplinary Sciences, Yokohama National University, Tokiwadai 79-5, Yokohama 240-8501, Japan*

[4] *Faculty of Engineering, Yokohama National University, Tokiwadai 79-5, Yokohama 240-8501, Japan*

(Received 31 March 2024; revised 12 July 2024; accepted 22 August 2024; published 13 September 2024)

This work presents a significant advancement in spin-wave computing devices utilizing magnetostatic surface spin waves. We demonstrate a micro-Y-shaped waveguide fabricated from yttrium iron garnet with a nanometer thickness. This intricately engineered design enables a novel logic device with two inputs and one output, enabling future cascading of such elements. Electrical measurements on the Y-shaped structure reveal that strategically introduced gaps effectively manipulate spin-wave propagation, as corroborated by detailed micromagnetic simulations. Notably, we achieve robust diagonal spin-wave transmission across 1.2 μm gaps, covering a distance of 120 μm. Furthermore, the gapped device exhibits clear phase-dependent spin-wave interference, surpassing the performance of a conventional Y-shaped design. This phenomenon, confirmed by mapping simulated magnetization components, signifies the potential of dipole-coupled devices for realizing efficient 2-input-1-output magnonic logic elements, laying the groundwork for future development in this field.

DOI: 10.1103/PhysRevApplied.22.034037

I. INTRODUCTION

The rapidly evolving field of magnonics holds immense promise for next-generation information processing, particularly in spin-wave computing [1–5]. Magnons, the quanta of spin waves, offer the potential for low-power data processing due to their noncharged nature. Significant strides have been made in realizing diverse magnonic functionalities, including the magnon transistor [6,7], majority gate [8], logic operations [9–11], multiplexers [12,13], and mode interconversion [14,15], by employing highly anisotropic spin-wave dispersion relations. Crucially, spin-wave interference within micro- or nano-scale circuits underpins all these functionalities [16,17]. However, a major challenge for spin-wave computing revolves around controlling spin-wave propagation within finite-size micro- and nano-circuits. This introduces undesirable wave confinement and local edge modes [18–21], which readily lead to signal disturbances by distorting the wave front and diminishing the ON:OFF ratio of spin-wave interference.

Recent research on spin-wave propagation in dipole-coupled networks offers a promising approach for manipulating spin waves with minimal wave front distortion [22–25]. By harnessing the magnetic dipole coupling between magnetic nanowires, researchers have demonstrated the potential for designing half-adder circuits based on this principle using Brillouin light scattering spectroscopy [23,24]. This approach represents a stepping stone toward complex logic circuits, such as full adders. Importantly, materials with low saturation magnetization (M_s), such as yttrium iron garnet (YIG), are found to be suitable options for spin-wave propagation via dipole coupling. Voltage-controlled magnetic anisotropy emerges as a promising choice for the input method due to its voltage-driven nature, leading to potentially lower power consumption compared with traditional methods [26–28]. Theoretical predictions suggest a significant reduction in power consumption compared with complementary metal-oxide-semiconductor (CMOS) devices [25]. Additionally, the compatibility of electrically driven spin-wave propagation with existing CMOS chips presents a significant advantage. However, a crucial gap remains – the experimental demonstration of spin-wave interference mediated by magnetic dipole coupling has yet to be achieved.

In this work, we present the electrical realization of spin-wave interference mediated by magnetic dipole-dipole coupling. This achievement is accomplished using micro-fabricated YIG waveguides strategically patterned with

*Contact author: sekiguchi-koji-gb@ynu.ac.jp

gaps to investigate the influence of dipole-coupling effects. The YIG microstructures were fabricated by employing radio frequency (rf) magnetron sputtering. Utilizing real-time propagating spin-wave spectroscopy, we observed distinct spin-wave interference signatures. The introduction of gaps demonstrably modulated spin-wave propagation, resulting in propagation delays and a reduction in resonance frequency. Notably, robust diagonal spin-wave transmission across 1.2 μm gaps was achieved, with propagation distances exceeding 120 μm. This work unveils a critical finding: the strategic incorporation of gaps within a micro-YIG structure, leveraging magnetic dipole coupling, holds significant potential for enhancing the ON:OFF ratio of magnonic devices. This paves the way for the development of magnonic logic elements based on spin waves, with potential applications in two-input, one-output computing architectures.

II. RESULTS AND DISCUSSION

Figure 1 presents a schematic of the experimental setup. The spin-wave waveguide consists of a 115-nm YIG thin film sputtered onto a gadolinium gallium garnet (GGG) substrate. To characterize the magnetic properties of the YIG film, ferromagnetic resonance (FMR) and microwave transmission experiments were conducted using a vector network analyzer (VNA, Agilent Technology E8362C). Figure 1(a) depicts coplanar waveguide (CPW) antennas fabricated on the YIG film for the VNA-FMR experiment. These antennas, composed of Ti (5 nm)/Au (50 nm), were designed to match the characteristic impedance of 50 Ω. Figure 1(b) shows the magnetic field (H) dependence of the ΔS_{21} parameter, revealing a two-dip absorption structure in the FMR resonance – a primary dip and a satellite dip. This phenomenon is attributed to impurities, such as non-Fe^{3+} ions, and the formation of nongarnet phases within the YIG film, as reported previously [29]. By fitting a Lorentzian function to the primary dip, we extracted the resonance frequency (f) and full width at half maximum (FWHM) (Δf), as shown in Figs. 1(c) and 1(d). The Kittel formula $\left(f = \gamma\sqrt{H(H+4\pi M_s)}\right)$, where f, $\gamma = 2.78$ MHz/Oe, H, and M_s represent the resonant frequency, gyromagnetic ratio, external magnetic field, and saturation magnetization, respectively, was employed to determine the saturation magnetization. This calculation yielded a value of $4\pi M_s = 1057$ G. Furthermore, by applying the broadening-damping relation ($\Delta f = 2\alpha f + f_0$) [30] to the data in Fig. 1(d), we were able to assess the magnitude of magnetic damping. In this equation, Δf represents the resonance linewidth, α is the Gilbert damping parameter, and f_0 signifies the natural resonance frequency. This analysis yielded a magnetic damping coefficient of $\alpha = 1.35 \times 10^{-3}$. Notably, the saturation magnetization ($4\pi M_s = 1057$ G) of the YIG thin film fabricated in this study is considerably lower compared with the reported value for the bulk YIG (approximately 1750 G) [31]. As previously mentioned, this lower M_s is advantageous for achieving dipole-mediated spin-wave propagation. Although the damping coefficient is not exceptionally low, it remains sufficiently low, being roughly an order of magnitude smaller than that of a ferromagnetic metal like Py. As shown in Appendix A, our experimental results indicate that spin-wave propagation through the gap was not observed in YIG waveguides with both smaller and larger M_s values (samples A and D). This observation may be attributed to the Y-shaped configuration of our experiment, where the spin-wave wavevector and the coupling region are not strictly parallel.

Figure 1(e) depicts the antennas deposited on the YIG thin film for the microwave transmission experiment designed to detect spin-wave propagation. The asymmetric CPW waveguides were spaced $D = 50$ μm apart. An external magnetic field, applied parallel to the antennas, excites magnetostatic surface spin waves (MSSWs). Figure 1(f) shows the ΔS_{21} parameter as a function of the external magnetic field. The transmission spectrum exhibits frequency shifts due to variations in the applied field. The relationship between the resonance frequency of the transmission spectrum and the external magnetic field is presented in Fig. 1(g). By fitting the data with the MSSW dispersion relation, we obtained a wave number of $k = 0.375$ rad/μm. The calculation employed the previously determined saturation magnetization ($4\pi M_s = 1057$ G) and film thickness ($d = 115$ nm). As the group velocity (v_g) of spin waves can be calculated using $v_g = \partial f/\partial k = D\delta f$ [30,32], where δf represents the period of oscillations in the inset of Fig. 1(h) and D is the propagation distance, we investigated the external magnetic field dependence of v_g, as shown in Fig. 1(h). Based on Fig. 1(h), we determined that an external magnetic field below 150 Oe is necessary to maintain a sufficiently large group velocity for subsequent experiments.

Figure 2(a) shows the Y-shaped YIG device with a 1.2-μm gap, fabricated using the Ar ion milling method. The two arms on the top side function as input waveguides, directing spin waves toward the central region. The bottom arm serves as the output waveguide, collecting the propagating spin waves. As shown in Fig. 2(b), the angle of the arms was designed to be 35° for optimal spin-wave propagation. Three Ti(5 nm)/Au(120 nm) antennas were deposited on the YIG waveguide using the lift-off technique. The width of the YIG waveguide in contact with the detection antennas was set at 40 μm for both the output and input waveguides. The central YIG waveguide, where the spin-wave interacts with the dipole-coupling effect, has a narrower width of 12 μm. Figures 2(c) and 2(d) illustrate the reference waveguides employed to isolate the impact of dipolar coupling. For clarity, reference waveguide 1 will be hereafter referred to as RW1, and reference waveguide 2 as RW2. RW1 features a straight, continuous design with no

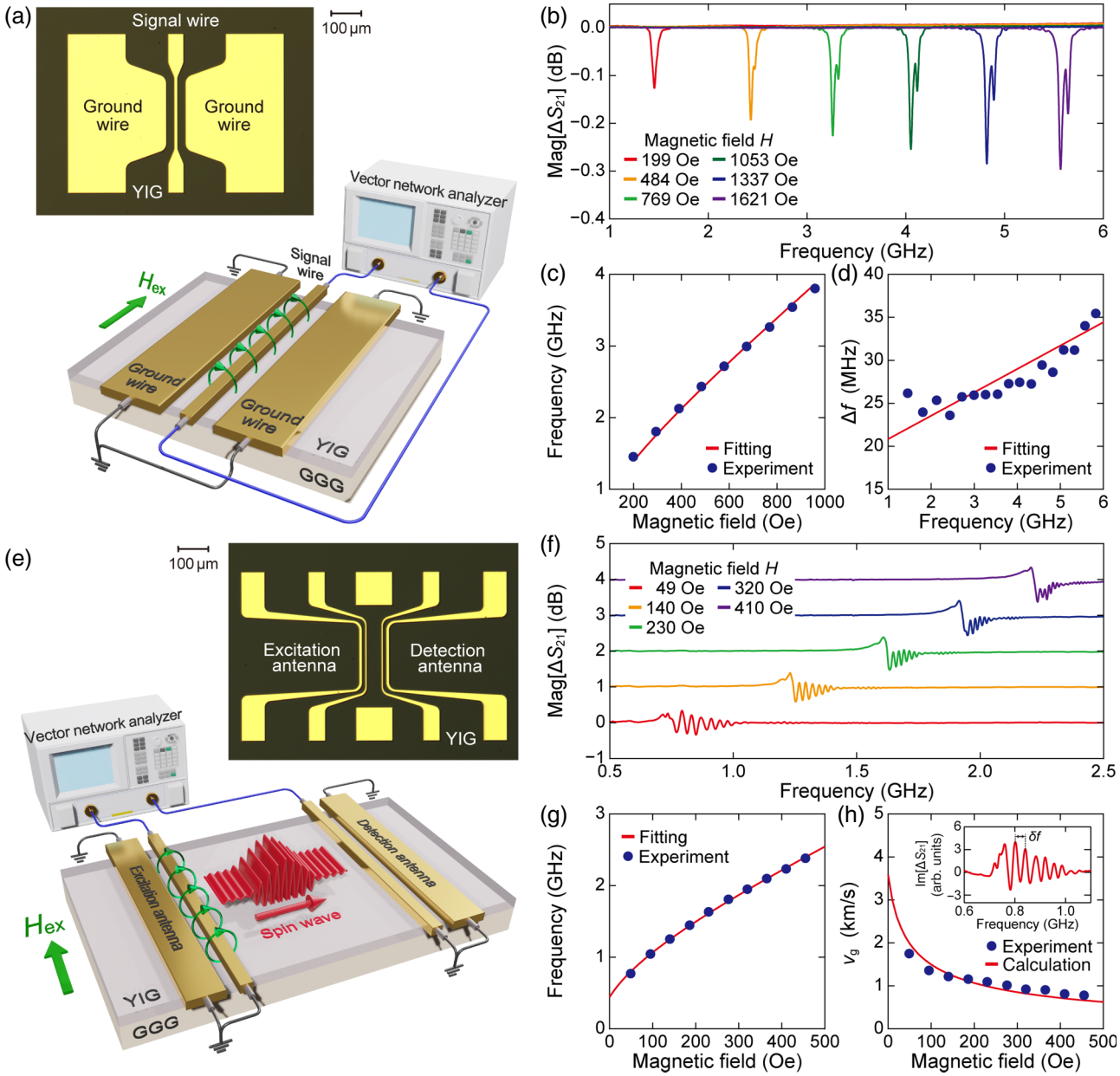

FIG. 1. Experimental details of the spin-wave propagation in YIG samples with reduced saturation magnetization. (a) Experimental setup for evaluating the magnetic characteristics of the sputtered YIG film. (b) Ferromagnetic resonance (FMR) spectra (ΔS_{21}) of sputtered YIG film as a function of external magnetic field. Magnetic field dependence of (c) resonant frequency f and (d) full width at half maximum (FWHM, Δf). (e) Experimental setup for propagating spin-wave spectroscopy. (f) Spin-wave spectra (ΔS_{21}) detected by vector network analyzer (VNA). (f) Magnetic field dependence of the MSSW resonant frequency. (h) Magnetic field dependence of its group velocity v_g. The inset shows a period for a spectrum that is used for the calculation of the group velocity. The solid lines represent theoretical fitting lines.

gaps or kinks. In contrast, RW2 lacks gaps but incorporates a kink to prevent the backflow of input spin waves.

Spin-wave generation, as depicted in Fig. 2(e), employed pulse-modulated sinusoidal microwaves from a precision signal generator (Hewlett Packard 83732B). Each pulse possessed a duration of 25 ns and a power level of −5 dBm. To introduce a phase difference ($\Delta\varphi$) between the two inputs, a series connection of three-phase shifters (APItech 6705 K, ARRAinc 6425E, and ARRAinc 6425E) was connected to one of the input antennas. The resulting interfered spin-wave signal was amplified using an rf amplifier (Mini-Circuits, ZHL-4240W+) and was detected using a real-time oscilloscope (Agilent DSO80604B) via the detection antenna. An external

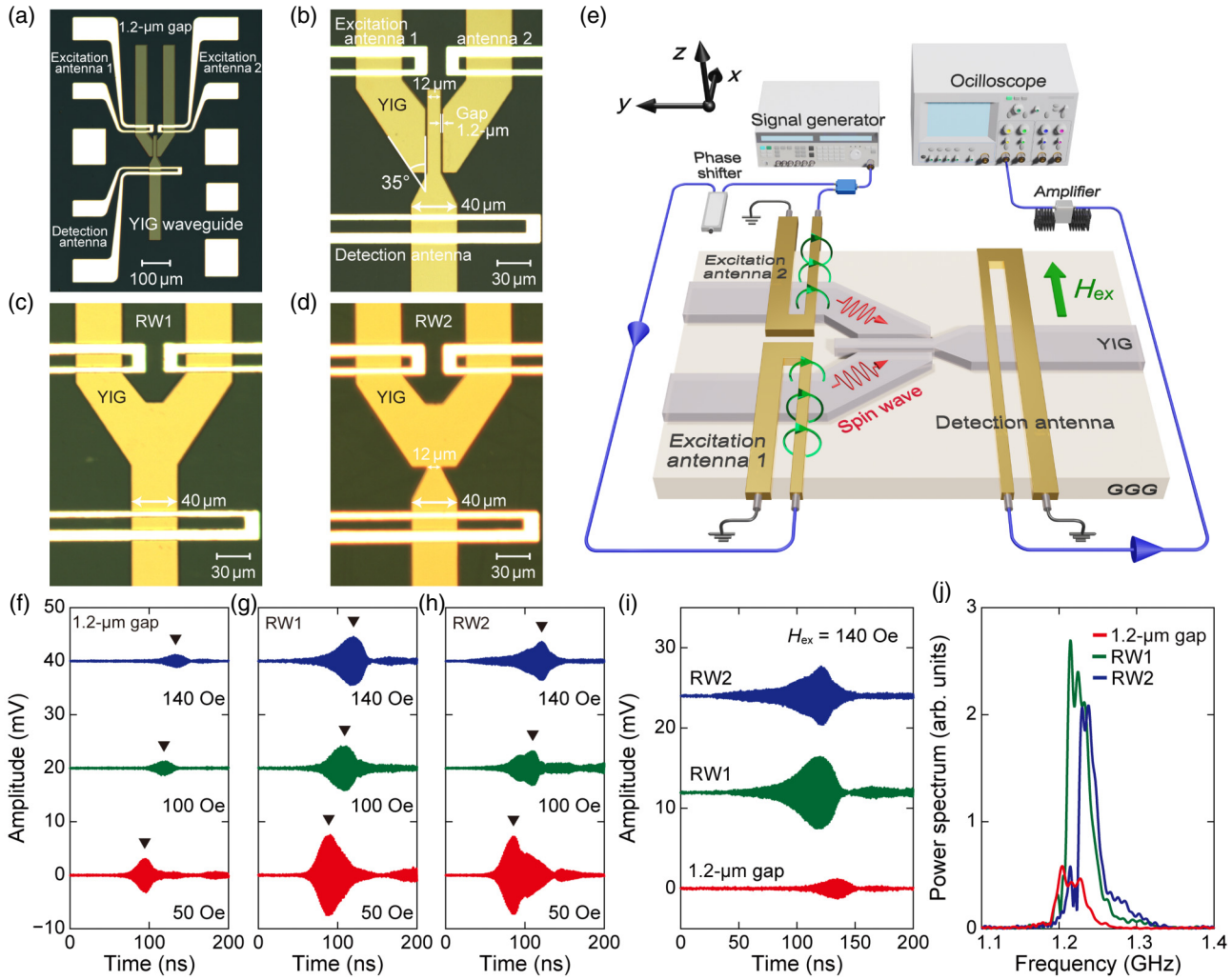

FIG. 2. Spin-wave propagation in several Y-shaped YIG samples. (a) Optical micrograph of a Y-shaped device with a 1.2-μm gap, and (b) an enlarged image at the dipole-coupling junction. (c),(d) Optical micrographs of reference Y-shaped devices (RW1 and RW2) without a gap. (e) Experimental setup for spin-wave propagation. Spin waves are excited by a signal generator and detected by a real-time oscilloscope. An external magnetic field was applied normal to the sample lines. Magnetic field dependence of time-domain wave packets for (f) the device with a 1.2-μm gap, (g) RW1, and (h) RW2 at an arbitral phase difference ($\Delta\varphi$). (i) Arrival time difference at H_{ex}= 140 Oe between the device with a 1.2-μm gap, RW1, and RW2. (i) Power spectra of time-domain waveforms showing the frequency difference of carrier packets at H_{ex} = 140 Oe between the device with a 1.2-μm gap, RW1, and RW2.

magnetic field, applied perpendicular to the input antenna, excited the MSSWs. Figure 2(f) illustrates the propagating spin-wave packet within the YIG waveguide with gaps at different magnetic field values (50, 100, and 140 Oe). An arbitrary phase difference ($\Delta\varphi$) was set for this demonstration. As the magnetic field increases, a delay in the arrival time of the packets is observed. It is important to note that, within this experimental setup, only the relative time difference between packets is valid, not the absolute origin of time. The measured time differences between arrivals were $\Delta t_1 = 24.3$ ns ($t_{50\text{Oe}} - t_{100\text{Oe}}$) and $\Delta t_2 = 15.3$ ns ($t_{100\text{Oe}} - t_{140\text{Oe}}$). Propagating spin-wave spectroscopy was similarly employed for RW1 and RW2, as shown in Figs. 2(g) and 2(h).

Figure 2(i) presents the time-domain measurement results for all three devices at an external magnetic field (H_{ex}) of 140 Oe. We compared the peak-to-peak voltage (V_{pp}) of the spin-wave signals for the device with a 1.2-μm gap, RW1, and RW2. The amplitude of the 1.2-μm gap device was found to be 0.28 times that of RW1 and 0.34 times that of RW2. Additionally, the difference in arrival times (Δt) between the device with the gap and the reference devices was 14.7 ns for RW1 and 14.2 ns for RW2. The introduction of the gap effectively narrows the waveguide and increases the demagnetization fields within the structure. This reduction in the effective magnetic field (H_{eff}) leads to a decrease in the spin-wave frequency (f). Consequently, the group velocity ($v_g = \partial f / \partial k$) is reduced,

resulting in the observed delays in arrival times. As shown in Fig. 2(j), the power spectra of the time-domain packets reveal a decrease in the peak frequency (f_p) for the devices with the 1.2-μm gap compared with both RW1 (15 MHz shift) and RW2 (35 MHz shift). These observed frequency shifts and amplitude reductions provide strong evidence that the spin waves propagated through the gaps via dipolar magnetic fields.

Figures 3(a)–3(c) depict the interfered spin-wave packet for each device at an external magnetic field (H_{ex}) of 140 Oe and a sinusoidal pulse frequency (f) of 1.23 GHz. The phase difference ($\Delta\varphi$) between the two-input antennas was set to either 0 or π. As shown in Fig. 3(a), single-sided excitation using antenna 2 alone resulted in a spin-wave amplitude of 1.57 mV (shown in a red waveform). When $\Delta\varphi$ was set to 0 (constructive interference), the spin-wave amplitude increased to approximately 2.65 mV, roughly 1.7 times higher than single-sided excitation. Conversely, at $\Delta\varphi = \pi$ (destructive interference), the spin-wave amplitude significantly decreased to about 0.28 mV, which is approximately one-sixth of the single-sided excitation level. Figure 3(d) illustrates the relationship between the maximum spin-wave amplitude and the continuously varied phase difference ($\Delta\varphi$). The data was fitted using the formula $A = \sqrt{A_1^2 + A_2^2 + 2A_1A_2\cos\Delta\varphi}$, where A_1 and A_2 represent the amplitudes of the independent input waves. As evident from Fig. 3(d), the device with the 1.2-μm gap, which utilizes magnetic dipole coupling, exhibits good agreement with the fitting curve. However, for RW1 and RW2, significant deviations between the fitting and experimental data are observed around $\Delta\varphi = \pi$, as indicated in the plot. The fitting curves consistently yielded $A = 0$, while RW1 and RW2 exhibited finite amplitudes of approximately $A_{RW1} = 1.79$ mV and $A_{RW2} = 1.35$ mV, respectively. Table I summarizes the ratio of spin-wave amplitudes at $\Delta\varphi = 0$ and $\Delta\varphi = \pi$ for all devices. The device with the 1.2-μm gap demonstrates the largest amplitude ratio, exhibiting approximately 1.6 and 1.7 times higher values compared with RW1 and RW2, respectively. This translates to the largest ON:OFF ratio observed in this experiment.

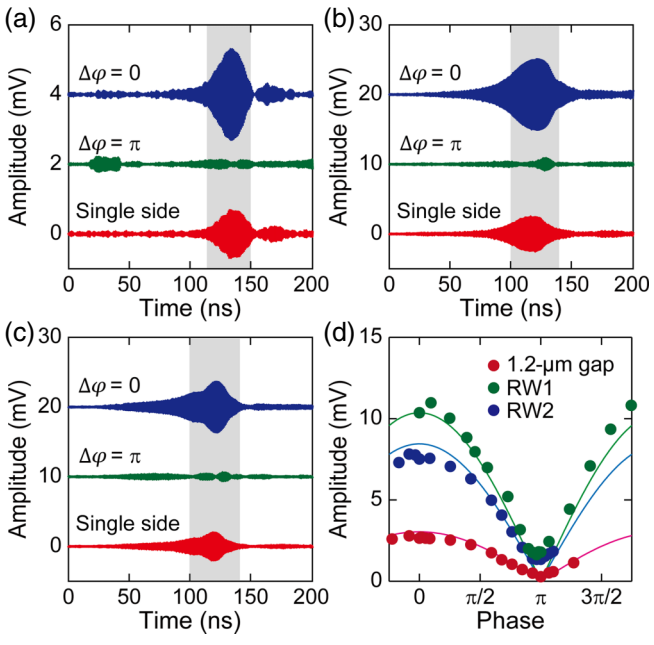

FIG. 3. Spin-wave interference via dipole coupling. Time-domain waveforms observed (a) in the device with a 1.2-μm gap, (b) in RW1, and (c) in RW2 under the conditions of $\Delta\varphi = 0$ and $\Delta\varphi = \pi$. Both constructive and destructive interferences are observed. (d) Phase dependence of the amplitude of interfered spin wave for three different devices.

TABLE I. Amplitudes of the interfered spin waves and their ratio.

Device	$A(\Delta\varphi = 0)$ mV	$A(\Delta\varphi = \pi)$ mV	$A(\Delta\varphi = 0)/A(\Delta\varphi = \pi)$
1.2-μm gap	2.65	0.28	9.46
RW1	10.36	1.79	5.78
RW2	7.52	1.35	5.57

Considering the device as a 2-input, 1-output logic element, we can encode digital information. A sine pulse wave, $A\sin(\omega t)$, can represent a logic "0," while a sine pulse wave with a π phase shift, $A\sin(\omega t + \pi)$, can represent a logic "1" for input values A and B. In our electrical measurements of the fabricated device with a 1.2-μm gap, we defined the threshold voltage as half of the maximum amplitude value ($V_{max}/2$). When the output voltage exceeds the threshold voltage, it is considered a "1," while a value below the threshold is considered a "0" [Appendix B]. With this encoding scheme, the absence of a phase difference between signals A and B leads to constructive interference, maximizing the output amplitude and corresponding to a logic "1." Conversely, a phase difference ($\Delta\varphi$) of π between signals A and B results in destructive interference, minimizing the output amplitude and corresponding to a logic "0." Based on these observations, we can conclude that the fabricated device and the employed electrical measurements demonstrate the potential for constructing an XNOR gate.

To gain a deeper understanding of a large ON:OFF ratio in dipole-coupled architecture, micromagnetic simulations were performed by numerically solving the Landau–Lifshitz–Gilbert equation, $\partial\mathbf{m}/\partial t = -\gamma_g\mu_0\mathbf{m}\times\mathbf{H}_{eff} + \alpha_G\mathbf{m}\times\partial\mathbf{m}/\partial t$, using MuMax3 [33]. In this equation, $\mathbf{m}$ represents the unit vector along the magnetization, $\mathbf{H}_{eff}$ is the effective magnetic field component, including exchange, magnetostatic, and external magnetic fields, and α_G represents the Gilbert damping constant. The simulated YIG thin film was modeled with a unit cell size of $400 \times 400 \times 57.5$ nm. The material parameters used

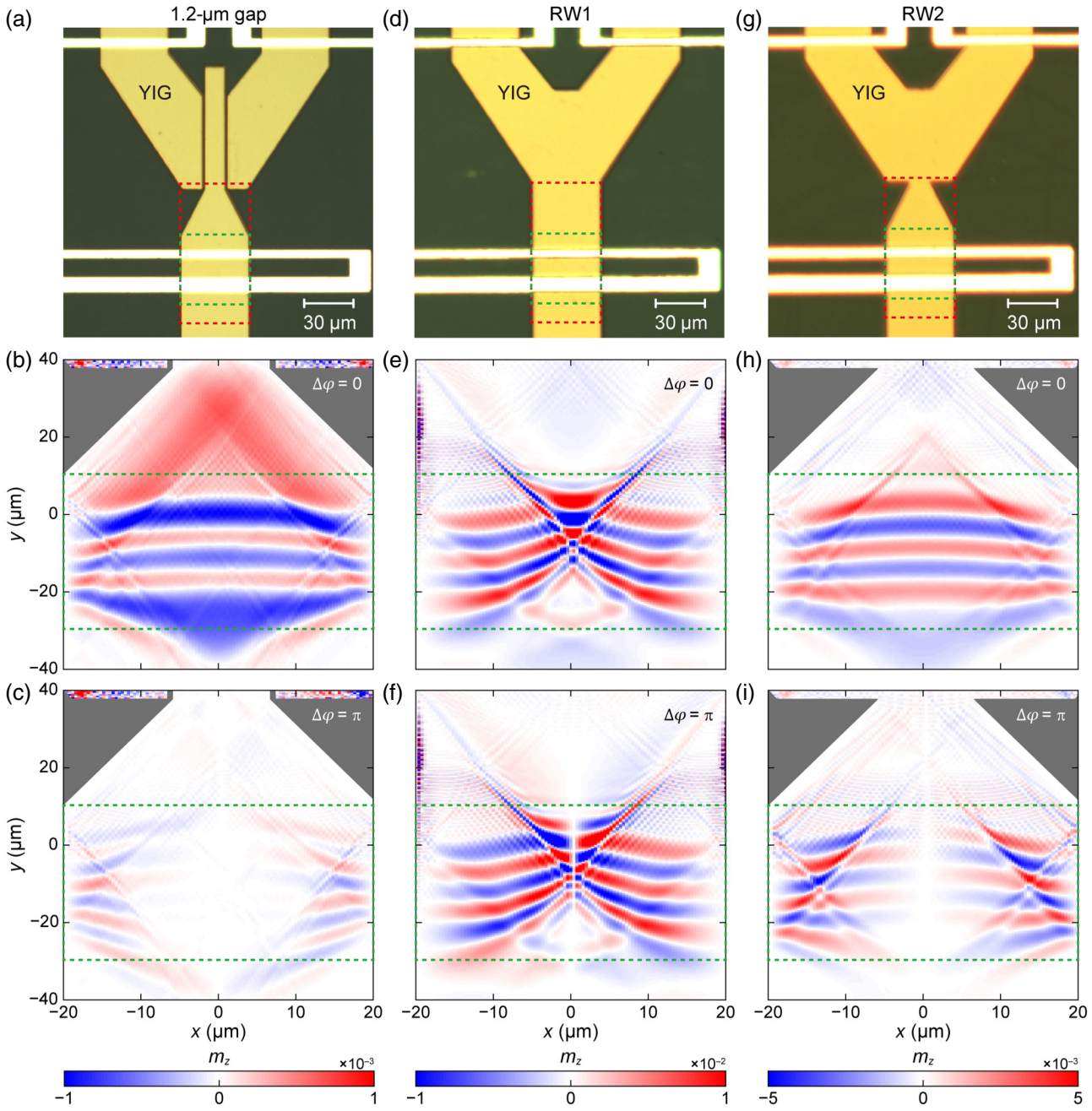

FIG. 4. Simulated wave fronts at the junctions of three different Y-shaped devices. The spin-wave wave front at the junction of (a) the device with a 1.2-μm gap for (b) $\Delta\varphi = 0$ and (c) $\Delta\varphi = \pi$. The intensity has a magnitude of m_z. The spin-wave wave front at the junction of (d) the RW1 for (e) $\Delta\varphi = 0$ and (f) $\Delta\varphi = \pi$. The spin-wave wave front at the junction of (g) the RW2 for (h) $\Delta\varphi = 0$ and (i) $\Delta\varphi = \pi$.

in the simulation were chosen to match the microfabricated YIG film: saturation magnetization $4\pi M_s = 1057$ G, Gilbert damping constant $\alpha_G = 1.35 \times 10^{-3}$, and exchange stiffness constant $A_{ex} = 3.7$ pJ/m. The values of the external magnetic field and excitation pulse in the simulations were identical to those employed in the experimental measurements ($H_{ex} = 140$ Oe and $f = 1.23$ GHz).

Figure 4 depicts the simulated wave front after it propagates beyond the coupled region of the waveguide in each device. The simulations analyzed the spatial distribution of the out-of-plane magnetization component (m_z) at a specific time point ($t = 125$ ns) after excitation. Figure 4(a) shows the device with a 1.2-μm gap and the analyzed region indicated by the red dotted square. Figure 4(b) presents the magnitude of magnetization (m_z) as a color map for a phase difference ($\Delta\varphi$) of 0 at the input. In contrast, Fig. 4(c) illustrates the scenario with a phase difference ($\Delta\varphi$) of π at the input. As evident from Fig. 4(b),

constructive interference occurs when $\Delta\varphi = 0$. This results in a single, uniform wave front propagating parallel to the negative y-direction. The two spin waves effectively merge into one coherent wave as they travel through the waveguide. Conversely, Fig. 4(c) shows destructive interference for $\Delta\varphi = \pi$. Here, the collision of the two waves leads to their weakening, evident from the significantly reduced intensity of the out-of-plane magnetization (m_z) observed in the color map.

Figure 4(d) represents the device of RW1 and the analyzed region (red dotted square). Figure 4(e) depicts the wave front in RW1. Unlike the device with a 1.2-μm gap, the two spin waves in RW1 collide without converging into a single wave front. Instead, they maintain their individuality, propagating with a noticeable diagonal component relative to the waveguide direction. Furthermore, Fig. 4(f) shows that even for $\Delta\varphi = \pi$ (destructive interference), the waves in RW1 remain distinct with no significant decrease in the overall intensity of the interference pattern, as illustrated by the color map. In contrast, Fig. 4(h) presents constructive interference in RW2 for $\Delta\varphi = 0$. Similar to the device with a 1.2-μm gap, a single, uniform wave front propagates parallel to the negative y-direction. The two waves effectively merge into one coherent wave front within the waveguide. However, a key distinction from the 1.2-μm gap device is observed in Fig. 4(i). Unlike the significant decrease in wave intensity for $\Delta\varphi = \pi$ in the gap device [Fig. 4(c)], RW2 exhibits two independent waves with intensities comparable with those at $\Delta\varphi = 0$. These waves persist even under destructive interference conditions.

To quantify the ON:OFF ratio, we calculated the spatial integral of the out-of-plane magnetization component (m_z^2) within the designated 40 μm × 40 μm region, outlined by the green dashed lines in Fig. 4. The calculated values are summarized in Table II. The device with the 1.2-μm gap exhibited a significant improvement in the ON:OFF ratio compared with both RW1 and RW2. Specifically, it demonstrated a 23.6-fold increase over RW1 and a 15.7-fold increase over RW2. While RW1 possesses a continuous Y-shaped structure and RW2 features a narrowed waveguide, the enhanced ON:OFF ratio achieved in this magnonic computing device can be attributed to the presence of the gap. This improvement likely arises from the efficient extraction of the spin-wave signal from the central region at $(x, y) = (0, 0)$, where the physical wave interference occurs. The gap effectively suppresses the contributions of reflected and diffracted waves at the junction.

TABLE II. Total sum of m_z^2 within the 40 μm × 40 μm region.

	$\Delta\varphi = 0$	$\Delta\varphi = \pi$	ON:OFF ratio
1.2-μm gap	1.79×10^{-3}	0.76×10^{-4}	23.6
RW1	0.16	0.16	1.0
RW2	2.08×10^{-2}	1.38×10^{-2}	1.51

To further investigate the ON:OFF ratio, we performed a Fourier transform analysis on the out-of-plane magnetization component (m_z) within the designated 40 μm × 40 μm region, outlined by the green dashed lines in Fig. 4. We focused on the $\Delta\varphi = \pi$ case, which represents the low signal (OFF) state. Figure 5(a) depicts the wavevector space distribution for the device with a 1.2-μm gap, while Figs. 5(b) and 5(c) show the distributions for RW1 and RW2, respectively. As shown in Fig. 5(a), the wavevector is concentrated on $k_x = \pm 0.02$ μm^{-1} (red color) and other weak wavevectors are confined within the region -0.26 μm$^{-1} < k_x < 0.26$ μm^{-1} and -0.23 μm$^{-1} < k_y < 0.23$ μm^{-1} (pink dotted rectangle). This means that the spin waves propagate in a straight line along the waveguide with an angle of less than $\theta = \pm\arctan(k_x/k_y) < 8.75°$. In contrast, for RW1 [Fig. 5(b)], the wavevector distribution extends to the region -0.55 μm$^{-1} < k_x < 0.55$ μm^{-1} and -0.33 μm$^{-1} < k_y < 0.33$ μm^{-1} (white dotted rectangle), although a similar intensity is still observed at $k_x = \pm 0.07$ μm^{-1}. A critical

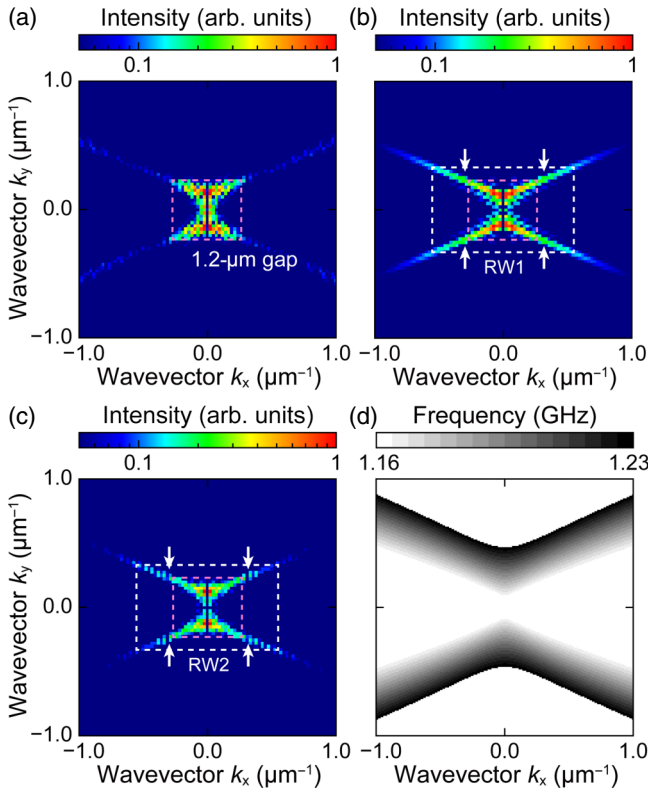

FIG. 5. Wavevector analysis of spin waves at the three different samples. The color maps depict normalized wavevector distributions obtained from simulation results for (a) the device with a 1.2-μm gap, (b) RW1, and (c) RW2. (d) Calculated wave number distribution of spin waves in a sample structure, utilizing the allowed spin-wave incidence angles derived from the sample structure and the dispersion relation of the spin waves.

difference is evident in the oblique intensity distributions indicated by the arrows. This suggests contributions from reflected or diffracted waves propagating with oblique angles $\theta = \pm\arctan(k_x/k_y) = 59°$. These unwanted waves could contribute to background noise in the OFF state for RW1 since it induces insufficient destructive interference.

Furthermore, Fig. 5(c) reveals another key distinction between RW1 and RW2. While RW2 also exhibits signal intensity for finite k_x components (oblique propagation), the region of such oblique intensity is significantly weaker compared with RW1. This suggests that RW2 possesses a cleaner wavevector distribution in the OFF state, potentially leading to a lower noise level. The kink structure in RW2 effectively reduces the contribution of reflection or diffraction waves. For reference, Fig. 5(d) depicts the theoretically calculated wavevector distribution, where the color intensity represents the magnitude of the frequency. It is important to consider that injected spin waves in Y-shaped devices typically have a finite injection angle (e.g., 35°). Consequently, the spin waves in the junction area possess both k_x and k_y components. Notably, the overall shape of the dispersion relation in Fig. 5(d) aligns well with the experimental observations presented in Figs. 5(a)–5(c). This agreement provides strong validation that the Fourier transform analysis has effectively captured the signal intensity within the wavevector space of the acquired region.

The wavevector analysis in Fig. 5 reveals a critical distinction between the devices. The device with a 1.2-μm gap utilizing dipole coupling exhibits a concentrated distribution of wavevector components (k_x) perpendicular to the spin-wave (MSSW) propagation direction, centered around $k_x = 0$ [Fig. 5(a)]. In contrast, RW1 and RW2 show a broader distribution with high intensities near $k_x = \pm 0.5$ μm^{-1} [Figs. 5(b) and 5(c)]. This observation suggests that the gap formation in the 1.2-μm gap device effectively suppresses the influx of waves propagating obliquely within the waveguide. By restricting the wavevector components in the waveguide width direction, the gap formation likely contributes to the improved ON:OFF ratio observed in the magnonic device.

III. CONCLUSION

In summary, this study demonstrates an innovative approach to spin-wave logic devices by incorporating a dipole-coupling gap into a micro-Y-shaped waveguide. The device design enables a simple 2-input-1-output magnonic logic functionality, which was realized by carefully balancing low saturation magnetization and magnetic damping in a thin yttrium iron garnet (YIG) film fabricated using a sputtering method. Time-domain electrical measurements revealed the gap's influence on spin-wave propagation and interference, leading to the successful detection of diagonally propagating spin waves over a distance of 120 μm. Notably, the ON:OFF ratio achieved a 1.7-fold improvement in the experiment and a 23-fold improvement in the simulation, compared with a reference device without the gap. These findings strongly suggest that dipole-coupling gaps offer a promising strategy for significantly boosting the performance of magnonic logic devices.

The data supporting the findings of this study are available from the corresponding author upon reasonable request.

ACKNOWLEDGMENTS

This work was supported by Grants-in-Aid for Scientific Research (Grants No. 19H00861, No. 18H05346, and No. 22K18321) from the Japan Society for the Promotion of Science (JSPS). K. S. acknowledges the support of Grants-in-Aid for Scientific Research (Grant No. 20H05652).

R. H. and K. S. planned the experiments. R. H., S. N., and K. S. designed and prepared the samples and performed spin-wave interference measurements. R. H. performed the analysis of spin-wave interference via dipole coupling. R. H., S. N., and K. S. wrote the manuscript. All of the authors discussed the results.

The authors declare no competing financial interests.

APPENDIX A

1. Preparation of the sputtered YIG films

Figure 6 shows the result of the vibrating sample magnetometer (VSM) experiment for the evaluation of

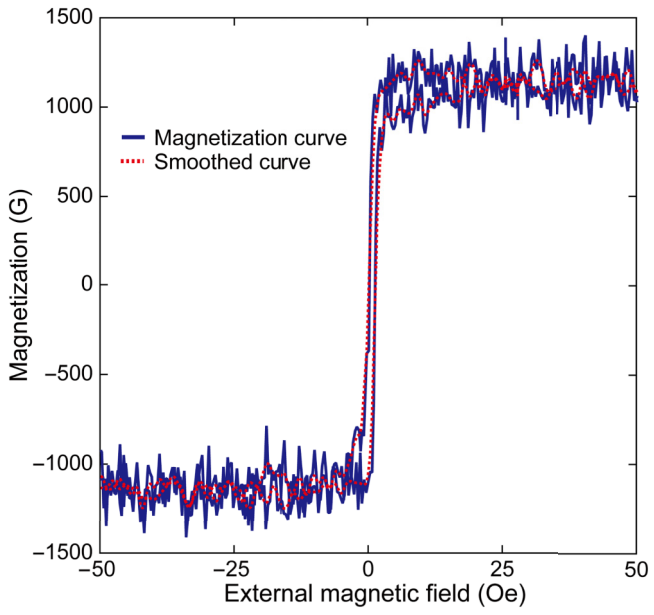

FIG. 6 Example of the VSM measurement. The magnetization of the YIG thin film was evaluated using VSM. The saturation magnetization is 1081 G on the application of an in-plane magnetic field.

TABLE III. YIG film fabrication and characterization.

	Sample A	Sample B	Sample C	Sample D
Ar pressure (Pa)	6.76	6.4	6.4	2.67
Annealing temp. (°C)	1000	1000	800	800
O_2 pressure ($\times 10^3$ Pa)	1.5	1.5	1.5	1.5
Thickness (nm)	44	115	115	120
Area roughness (nm)	0.31	0.36	0.67	0.14
	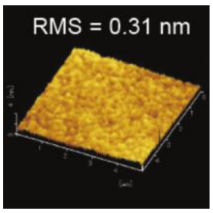	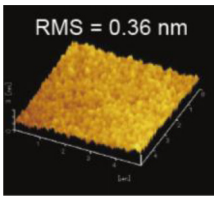	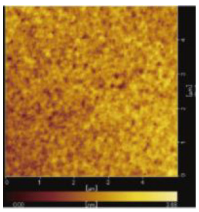	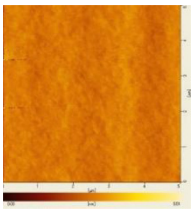
Magnetization (G)	849	1049	1057	1329
Damping factor ($\times 10^{-3}$)	1.99	1.36	1.35	0.446

magnetization. As shown, the saturation magnetization of sputtered YIG film was 1081 G on the application of an in-plane magnetic field and is approximately identical to the FMR measurement. Table III summarizes the sputtered YIG films with relatively small magnetizations. Under these sputtering and annealing conditions, we obtained very flat YIG films with smaller area roughness. Atomic force microscopy measurements revealed no specific grains formed. Successive FMR measurements revealed a correlation between the magnetization and damping factor. As shown in Table III, YIG films with a larger magnetization possess smaller damping factors, while those with smaller magnetization possess larger damping factors. In our Y-shaped waveguide with these films, only sample C exhibits clear dipolar-mediated spin-wave propagation. There is room for design optimization of the dipolar coupling regime since the Y-shaped sample contains a small overlap region. By modifying the sample geometry, it may be possible to observe propagation even in samples with larger magnetizations.

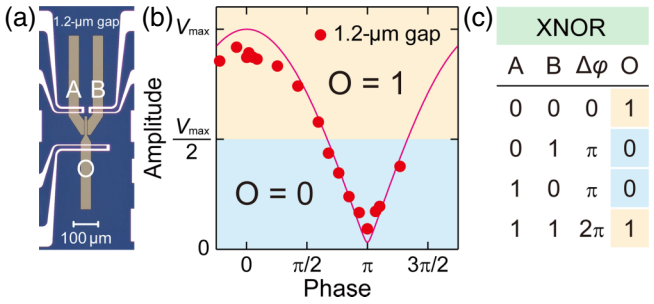

FIG. 7 XNOR truth table. Encoding scheme of the logic operation for the Y-shaped waveguide. (a) Sample geometry of the Y-shaped sample with a 1.2-μm gap. (b) Phase difference dependence of spin-wave interference between two different inputs. (c) Truth table of the XNOR operation.

APPENDIX B

1. Truth table for the XNOR operation

Figure 7(a) shows an encoding scheme for the Y-shaped gate [Fig. 7(a)]. The gate possesses two inputs (A and B) and one output (O). For example, for given inputs $A = A\sin(\omega t)$ and $B = A\sin(\omega t)$ where A and $\omega/2\pi$ are spin-wave amplitude and frequency, respectively, the output is expected to be $O = 2A\sin(\omega t)$. Assuming that "0" and "1" are encoded using phase information, the output should be $O = 0$ when the inputs are represented as $A = A\ \sin(\omega t)$ and $B = A\ \sin(\omega t + \pi)$. If the output "1" is defined as $V > V_{max}/2$ and the output "0" is defined as $V < V_{max}/2$, as shown in Fig. 7(b), the Y-shaped sample acts as an XNOR gate, as shown in Fig. 7(c). It is important to note that while the inputs are initially encoded using phase information, the output is encoded using the amplitude. As a result, the sample could be called a phase-amplitude converter.

[1] A. Barman, *et al.*, The 2021 magnonics roadmap, J. Phys.: Condens. Matter. **33**, 413001 (2021).
[2] A. V. Chumak, V. I. Vasyuchka, A. A. Serga, and B. Hillebrands, Magnon spintronics, Nat. Phys. **11**, 453 (2015).
[3] A. V. Chumak, *et al.*, Advances in magnetics roadmap on spin-wave computing, IEEE Trans. Magn. **58**, 0800172 (2022).
[4] K. Sekiguchi, K. Yamada, S. M. Seo, K. J. Lee, D. Chiba, K. Kobayashi, and T. Ono, Nonreciprocal emission of spin-wave packet in FeNi film, Appl. Phys. Lett. **97**, 022508 (2010).
[5] M. Iwaba and K. Sekiguchi, Spin-wave switching using dynamic magnonic crystal, Appl. Phys. Express **14**, 073002 (2021).
[6] A. V. Chumak, A. A. Serga, and B. Hillebrands, Magnon transistor for all-magnon data processing, Nat. Commun. **5**, 4700 (2014).

[7] K. Sekiguchi, The basis of magnon transistors, AAPPS Bull. **28**, 2 (2018).

[8] N. Kanazawa, T. Goto, K. Sekiguchi, A. B. Granovsky, C. A. Ross, H. Takagi, Y. Nakamura, H. Uchida, and M. Inoue, The role of Snell's law for a magnonic majority gate, Sci. Rep. **7**, 7898 (2017).

[9] T. Goto, T. Yoshimoto, B. Iwamoto, K. Shimada, C. A. Ross, K. Sekiguchi, A. B. Granovsky, Y. Nakamura, H. Uchida, and M. Inoue, Three port logic gate using forward volume spin wave interference in a thin yttrium iron garnet film, Sci. Rep. **9**, 16472 (2019).

[10] K. O. Nikolaev, D. Raskhodchikov, J. Bensman, E. Lomonte, L. Jin, R. Schmidt, J. Kern, S. Michaelis de Vasconcellos, R. Bratschitsch, S. O. Demokritov, W. H. P. Pernice, and V. E. Demidov, Operation of a submicrometer waveguide cross as a spin-wave logic gate, Appl. Phys. Lett. **123**, 142402 (2023).

[11] N. Sato, K. Sekiguchi, and Y. Nozaki, Electrical demonstration of spin-wave logic operation, Appl. Phys. Express **6**, 063001 (2013).

[12] K. Vogt, F. Y. Fradin, J. E. Pearson, T. Sebastian, S. D. Bader, B. Hillebrands, A. Hoffmann, and H. Schultheiss, Realization of a spin-wave multiplexer, Nat. Commun. **5**, 3727 (2014).

[13] Q. Wang, A. V. Chumak, and P. Pirro, Inverse-design magnonic devices, Nat. Commun. **12**, 2636 (2021).

[14] T. Eguchi, S. Nezu, Y. Naemura, and K. Sekiguchi, Spin-wave interconversion via thermoelectric point-contact control, Phys. Rev. Res. **4**, 033135 (2022).

[15] A. V. Sadovnikov, C. S. Davies, V. V. Kruglyak, D. V. Romanenko, S. V. Grishin, E. N. Beginin, Y. P. Sharaevskii, and S. A. Nikitov, Spin wave propagation in a uniformly biased curved magnonic waveguide, Phys. Rev. B **96**, 060401(R) (2017).

[16] M. Iwaba and K. Sekiguchi, Spin-wave enhancement using feedback-ring structure, Jpn. J. Appl. Phys. **62**, 103001 (2023).

[17] N. Sato, S. J. Lee, S. W. Lee, K. J. Lee, and K. Sekiguchi, Phase stability of magnonic logic operation in microfabricated metallic wires, Appl. Phys. Express **9**, 083001 (2016).

[18] V. E. Demidov, S. O. Demokritov, K. Rott, P. Krzysteczk, and G. Reiss, Self-focusing of spin waves in Permalloy microstripes, Appl. Phys. Lett. **91**, 52504 (2007).

[19] H. J. Jason Liu, A. Guerrero, K. E. Nygren, M. Swyt, and K. S. Buchanan, Spin wave wavevector up-conversion in Y-shaped Permalloy structures, Appl. Phys. Lett. **119**, 172403 (2021).

[20] P. Clausen, K. Vogt, H. Schultheiss, S. Schäfer, B. Obry, G. Wolf, P. Pirro, B. Leven, and B. Hillebrands, Mode conversion by symmetry breaking of propagating spin waves, Appl. Phys. Lett. **99**, 162505 (2011).

[21] S. Nezu, T. Scheike, H. Sukegawa, and K. Sekiguchi, Propagating backward-volume spin waves in epitaxial Fe films, AIP Adv. **12**, 035320 (2022).

[22] Q. Wang, P. Pirro, R. Verba, A. Slavin, B. Hillebrands, and A. V. Chumak, Reconfigurable nanoscale spin-wave directional coupler, Sci. Adv. **4**, e1701517 (2018).

[23] A. V. Sadovnikov, E. N. Beginin, S. E. Sheshukova, D. V. Romanenko, Y. P. Sharaevskii, and S. A. Nikitov, Directional multimode coupler for planar magnonics: Side-coupled magnetic stripes, Appl. Phys. Lett. **107**, 202405 (2015).

[24] A. V. Sadovnikov, S. A. Odintsov, E. N. Beginin, S. E. Sheshukova, Y. P. Sharaevskii, and S. A. Nikitov, Toward nonlinear magnonics: Intensity-dependent spin-wave switching in insulating side-coupled magnetic stripes, Phys. Rev. B **96**, 144428 (2017).

[25] Q. Wang, M. Kewenig, M. Schneider, R. Verba, F. Kohl, B. Heinz, M. Geilen, M. Mohseni, B. Lägel, F. Ciubotaru, C. Adelmann, C. Dubs, S. D. Cotofana, O. V. Dobrovolskiy, T. Brächer, P. Pirro, and A. V. Chumak, A magnonic directional coupler for integrated magnonic half-adders, Nat. Electron. **3**, 765 (2020).

[26] S. Miwa, M. Suzuki, M. Tsujikawa, K. Matsuda, T. Nozaki, K. Tanaka, T. Tsukahara, K. Nawaoka, M. Goto, Y. Kotani, T. Ohkubo, F. Bonell, E. Tamura, K. Hono, T. Nakamura, M. Shirai, S. Yuasa, and Y. Suzuki, Voltage controlled interfacial magnetism through platinum orbits, Nat. Commun. **8**, 15848 (2017).

[27] T. Maruyama, Y. Shiota, T. Nozaki, K. Ohta, N. Toda, M. Mizuguchi, A. A. Tulapurkar, T. Shinjo, M. Shiraishi, S. Mizukami, Y. Ando, and Y. Suzuki, Large voltage-induced magnetic anisotropy change in a few atomic layers of iron, Nat. Nanotech. **4**, 158 (2009).

[28] S. Miwa, K. Matsuda, K. Tanaka, Y. Kotani, M. Goto, T. Nakamura, and Y. Suzuki, Voltage-controlled magnetic anisotropy in Fe|MgO tunnel junctions studied by x-ray absorption spectroscopy, Appl. Phys. Lett. **107**, 162402 (2015).

[29] Y. XIe, Y. Yang, D. Liu, S. Chen, D. Gao, B. Tan, T. Gong, Q. Chen, L. Bi, T. Liu, and L. Deng, Optimizing the quality of epitaxial $Y_3Fe_5O_{12}$ thin films via a two-step post-annealing process, Cobot **1**, 19 (2022).

[30] H. Qin, S. J. Hämäläinen, K. Arjas, J. Witteveen, and S. Dijken, Propagating spin waves in nanometer-thick yttrium iron garnet films: Dependence on wave vector, magnetic field strength, and angle, Phys. Rev. B **98**, 224422 (2018).

[31] D. D. Stancil and A. Prabhakar, *Spin Waves: Theory and Applications* (Springer, USA, 2009).

[32] S. Neusser, G. Durr, H. G. Bauer, S. Tacchi, M. Madami, G. Woltersdorf, G. Gubbiotti, C. H. Back, and D. Grundler, Anisotropic propagation and damping of spin waves in a nanopatterned antidot lattice, Phys. Rev. Lett. **105**, 067208 (2010).

[33] A. Vansteenkiste, J. Leliaert, M. Dvornik, M. Helsen, F. Garcia-Sanchez, and B. V. Waeyenberge, The design and verification of MuMax3, AIP Adv. **4**, 107133 (2014).